ADVANCED OPTICAL MATERIALS
www.advopticalmat.de

Narrowband Monolithic Perovskite–Perovskite Tandem Photodetectors

*Lucía Martínez-Goyeneche, Lidón Gil-Escrig, Isidora Susic, Daniel Tordera, Henk J. Bolink, and Michele Sessolo**

Narrowband photodetectors (PDs) are sought after for many applications requiring selective spectral response. The most common systems combine optical bandpass filters with broadband photodiodes. This work reports a method to obtain a narrowband response in a perovskite PD by the monolithic integration of a perovskite photoconductor and a perovskite photodiode. The spectral response of the tandem PD is determined by the bandgap energy difference of the two perovskites, and exhibits a full width at half maximum below 85 nm, an external quantum efficiency up to 68% and a high specific detectivity of ≈10^{12} Jones in reverse bias, enabling the device to detect weak light signals. The absorption profile of the narrowband PD can be tuned by changing the thickness and bandgap of the wide bandgap perovskite absorber.

1. Introduction

Photodetectors (PDs) are optoelectronic devices that convert light into electrical signals, in the form of either current or voltage.[1] PDs have several applications in a variety of fields, such as image sensing, biological detection, surveillance, optical communications, and intelligent monitoring.[2–6] Some of these applications require achieving color discrimination and therefore selective wavelength photodetection.[7–11] According to the bandwidth of their spectral response window, PDs are generally classified as broadband (i.e., panchromatic) or narrowband (i.e., wavelength selective). Generally, narrowband PDs are realized by different strategies: combining broadband PDs with optical bandpass filters,[12] using a photoactive material with narrowband absorption[13] or by modulation of the light absorption in a specific wavelength range by means of plasmonic, grating, or microcavity effects.[14–18]

Semiconducting organic–inorganic (hybrid) lead halide perovskites have been widely applied in solar cells,[19] light-emitting diodes,[20] and PDs,[21,22] due to their tunable and favorable optoelectronic properties. Hybrid perovskites have been initially considered for photovoltaic cells, with rapid progress in power conversion efficiency from about 3% in 2009 up to 25.6% in 2021.[23,24] Recently, they have emerged as an attractive semiconducting material for PDs. Perovskites are promising for sensitive and fast light detection due to a combination of efficient light absorption, low dark current, and high charge carrier mobility.[25–27] The combination of a high optical absorption coefficient and a direct bandgap, however, makes perovskite PDs intrinsic broadband light detectors. One way to narrow the spectral response of broadband absorbers is via the use of thick semiconducting films in a process called charge collection narrowing (CCN). In a thick junction, high energy photons are absorbed close to the surface due to the high absorption coefficient, hence the photogenerated carriers will almost quantitatively recombine before reaching the external electrodes. On the other hand, low energy photons will be absorbed within the volume of the semiconductor (due to a lower absorption coefficient), with much reduced recombination losses leading to a high photoresponse. This principle has been demonstrated in organic semiconductor and later also in perovskite films.[28,29] CCN has also been applied to perovskite single-crystal PDs, where surface recombination is maximized as a consequence of the very thick semiconductor.[30] This approach has been widely adopted and investigated using single crystals or very thick (>100 µm) perovskite films.[8,25,31,32] While effective in narrowing the spectral response, the use of very thick films and especially of single crystals might reduce the application range (e.g., to flexible devices) and compromise speed. Thin film narrowband PDs have also been demonstrated using two perovskite thin films with different bandgaps, the wider bandgap used as an optical bandpass filter on the outer side (substrate) of the PDs, and the narrower bandgap perovskite being the active layer.[11,33] The wavelength and bandwidth of the photoresponse is hence defined by the optical absorption onset of the narrow bandgap absorber and the energy difference between the bandgap of the two materials. In this approach the wide

L. Martínez-Goyeneche, L. Gil-Escrig, I. Susic, D. Tordera, H. J. Bolink, M. Sessolo
Instituto de Ciencia Molecular
Universidad de Valencia
C/ Catedrático J. Beltrán 2, Paterna 46980, Spain
E-mail: michele.sessolo@uv.es

The ORCID identification number(s) for the author(s) of this article can be found under https://doi.org/10.1002/adom.202201047.

DOI: 10.1002/adom.202201047

bandgap perovskite is acting solely as a filter and is coated on the backside of the devices, which might limit their stability and integration with other technologies. This is due to the fact that in most practical applications of photodetectors (e.g., biomedical sensors or visible and X-ray imagers), there is a need to drive the devices by using a thin film transistor backplane which is fabricated directly on top of the (glass or flexible) substrate. The photodetector is processed on top of it and topped with a semitransparent electrode, such as sputtered indium tin oxide (ITO) or a very thin metal electrode.[34]

In this work, we propose an alternative method to obtain narrowband perovskite PDs by using a monolithic tandem structure with two electrically connected perovskite PDs. In particular, we fabricated a multilayer device with a wide bandgap (1.75 eV) $FA_{0.7}Cs_{0.3}Pb(I_{0.7}Br_{0.3})_3$ perovskite photoconductor, simultaneously acting as charge transport layer and optical filter, monolithically connected to a methylammonium lead iodide ($MAPbI_3$, 1.6 eV) photodiode. The monolithic integration is enabled by the use of thermal vacuum deposition for both the organic and the perovskite semiconductors.[35,36] Proof-of-concept PDs show a narrow spectral response centered in the near infrared (NIR, 730 nm) with a full width at half maximum (FWHM) of ≈80 nm, EQE up to 68% and high specific detectivity in reverse bias (≈10^{12} Jones in reverse bias).

2. Results and Discussion

We initially fabricated and characterized the isolated photodiodes with only one semiconductor using MAPI in a p-i-n configuration (**Figure 1**a). The characterization of the perovskite film is reported in Figure S1, Supporting Information. The structure of the device is ITO/TaTm:F_6-TCNNQ (40 nm)/TaTm (20 nm)/MAPI (500 nm)/C_{60} (50 nm)/BCP (8 nm)/Ag, where TaTm is *N*4,*N*4,*N*4″,*N*4″-tetra([1,1′-biphenyl]-4-yl)-[1,1′:4′,1″-terphenyl]-4,4″-diamine), F_6-TCNNQ is 2,2′-(perfluoronaphthalene-2,6-diylidene)dimalononitrile, C_{60} is fullerene and BCP is bathocuproine. The notation TaTm:F_6-TCNNQ indicates that the two materials are co-sublimed (F_6-TCNNQ at 10 wt%) in order to increase the conductivity of the film which is used as the hole injection layer (HIL).[37] All layers are deposited by thermal vacuum deposition, as previously reported and as described in the experimental section.[37,38]

Most of the perovskite PDs reported in literature are characterized in the photovoltaic mode (in short circuit condition, V = 0 V, or sometimes at mild reverse bias of up to –0.5 V). This is because at more negative voltage in perovskite thin film devices, ionic motion, electrochemical reactions and reverse bias breakdown can occur.[39–41] Moreover, the lower dark current at low bias voltage leads to a larger specific detectivity, compared to what would be obtained at more negative bias. However, most of driving electronics for commercial PDs requires negative reverse bias to increase the response time and the collection efficiency (typically between –1 and –5 V), hence the investigation and development of bias-robust perovskite PDs is highly sought-after.[42,43]

In view of this, the dark and photocurrent density versus voltage (J–V) characteristics of the photodiode were measured in a wide range, between –2 and 2 V (Figure 1b). The dark current density (J_D) at –1 V is 8×10^{-3} mA cm^{-2} and rises to 1.5×10^{-2} mA cm^{-2} at –2 V. The J–V curves have almost no

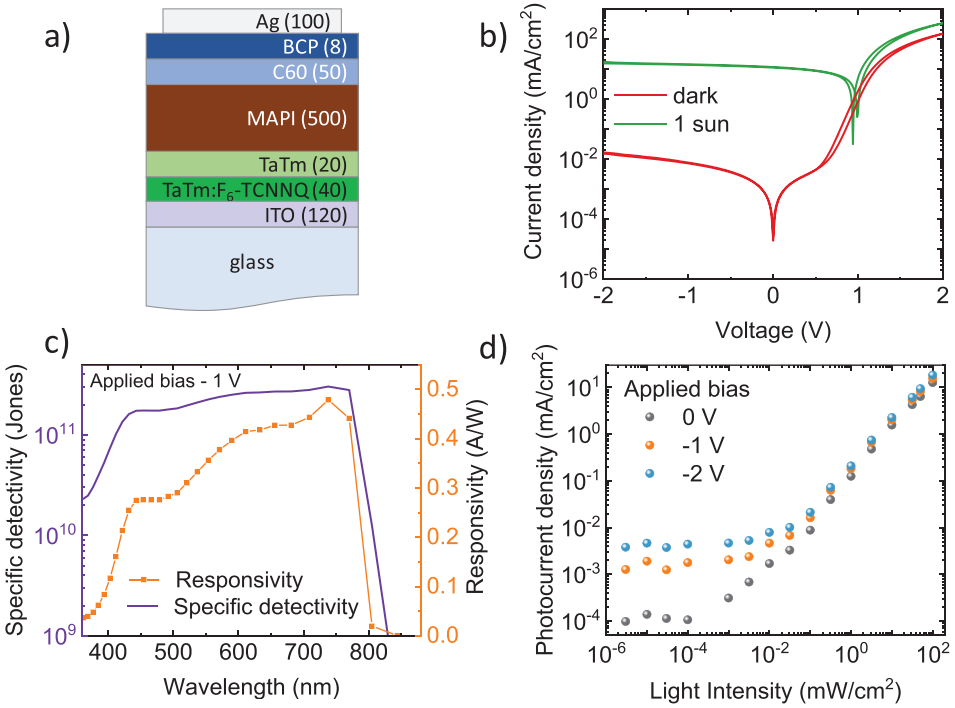

Figure 1. Characterization of MAPI photodiodes. a) Schematic device structure of the photodiode. b) J–V characteristics (–2 to 2 V) in dark (red curve) and under 100 mW cm^{-2} illumination (green curve). c) Responsivity (orange line and symbols) and specific detectivity (purple curve) at –1 V. d) Dynamic response of the photodiode at different applied bias voltages.

hysteresis and the devices display a good diode behavior (current rectification ratio of ≈10^4 in the −2 to 2 V range). This finding correlates with the very low hysteresis typically observed in vacuum-deposited perovskite solar cells, indicating that either ion migration or interface recombination (or both) are suppressed in these perovskite devices.[44,45] The *J*–*V* curves under 1 sun equivalent illumination (100 mW cm^{-2}) shows a current density of 14.7 mA cm^{-2} at −1 V and very small voltage dependence in the measured range of reverse bias. The diode under illumination shows an open circuit voltage (V_{oc}) of 1.1 V. The difference between the current in the dark and under illumination is of about three orders of magnitudes at −2 V.

The device responsivity (*R*) and the specific detectivity (*D**) measured with an applied voltage of −1 V are shown in Figure 1c. The responsivity is the ratio between the output photocurrent and the input light power, and is defined as:

$$R = \mathrm{EQE} \times \frac{e}{h\nu} \tag{1}$$

where EQE is the external quantum efficiency, *e* is the elementary charge, *h* is the Planck's constant and *ν* is the frequency of the incident light. The diode shows a broadband EQE in the wavelength range of 440 to 770 nm, with values of ≈80% which are independent of the applied bias voltages (between −2 and 0 V in 0.5 V step, Figure S2, Supporting Information). The maximum responsivity at −1 V is 0.48 A W^{-1}. The high EQE and responsivity indicate an efficient charge carrier generation and extraction in the photodiode.

Another key figure of merit that characterizes the performance of a PD is the specific detectivity (*D**). This parameter reflects the sensitivity of the device to detect weak levels of light. Although PDs work under reverse bias (negative voltage), most of the published perovskite PDs reports the specific detectivity at zero bias (photovoltaic regime). At zero bias, assuming that the main source that contributes to the noise is the thermal noise, the specific detectivity can be calculated using the following formula:

$$D^* = \frac{R\sqrt{A}}{i_{\mathrm{thermal}}} \tag{2}$$

where *A* is the photoactive area (here 0.0825 cm^2), and i_{thermal} is the thermal noise current expressed as $i_{\mathrm{thermal}} = \sqrt{4k_BT / R_{sh}}$ in which k_B is Boltzmann constant, *T* is temperature and R_{sh} is the shunt resistance extracted from the slope of the dark *I*–*V* curve around zero bias.[46] In general, a low dark current indicates large values of the shunt resistance and therefore a high specific detectivity. The specific detectivity of the photodiode at zero bias is 1.44×10^{12} Jones at 738 nm (Figure S2, Supporting Information), which is comparable to previously reported MAPI photodiodes characterized in photovoltaic mode.[47,48] In reverse bias, the formula of the specific detectivity can be simplified as:

$$D^* = \frac{R}{\sqrt{2eJ_d}} \tag{3}$$

At a reverse bias of −1 V, our photodiode has a maximum specific detectivity of 3.0×10^{11} Jones at 738 nm (Figure 1c), similar to previous reports using the same active material.[49] The linear dynamic range (LDR) describes the range in which the response of photocurrent versus light intensity is a linear function:

$$\mathrm{LDR} = 20 \log \frac{J_{\mathrm{upper}}}{J_{\mathrm{lower}}} \tag{4}$$

where J_{upper} and J_{lower} are the higher and lower light current limits in which the photocurrent is linear to the light intensity. For practical applications, having a large LDR means that the PD can operate in a wider range of lighting conditions. The LDR was measured by recording the photocurrent of the photodiode under 1 sun equivalent illumination (100 mW cm^{-2}) and by attenuating the intensity using neutral density filters. Figure 1d shows the photocurrent versus light intensity at different applied bias voltages (0, −1, and −2 V). The photodiode shows a linear response to incident light from ≈10^{-3} mW cm^{-2} to 10^2 mW cm^{-2} corresponding to a LDR of 92 dB at 0 V. When the negative applied bias is increased to −1 and −2 V, the linear response to incident light presents a different range (from 10^{-1} to 10^2 mW cm^{-2}), resulting in a lower LDR of 60 dB.

Narrowband PDs were prepared using the MAPI photodiode in series with a wide bandgap perovskite photoconductor. The photoconductor is deposited on the glass/ITO substrate and consists of a wide bandgap perovskite film of the type $FA_{0.7}Cs_{0.3}Pb(I_{0.7}Br_{0.3})_3$ (600 nm thick; characterization of the perovskite film is reported in Figure S1, Supporting Information) sandwiched in between two hole transport layers consisting of TaTm doped with F_6-TCNNQ (40 nm thick). The MAPI photodiode is monolithically fabricated on top with the same layout as previously presented (schematics in **Figure 2**a). Thanks to the use of vacuum deposition, this multilayer architecture can be readily obtained, as shown in the cross-section scanning electron microscopy (SEM) image in Figure 2b. The expected corresponding spectral response is determined by the bandgap difference of the two perovskites, which is rather small (1.6 and 1.75 eV, for MAPI and $FA_{0.7}Cs_{0.3}Pb(I_{0.7}Br_{0.3})_3$, respectively).[50,51] The perovskite layers are electrically connected in a tandem device architecture, where photogenerated holes within the MAPI film are transported through the wide bandgap perovskite film and extracted at the ITO electrode. The approximate flat band energy diagram for the materials used in the tandem devices is shown in Figure 2c. In principle, there is no energy barrier between the different layers of the device architecture, which should result in efficient transport and extraction of charge carriers at the electrodes. We initially tested an isolated photoconductor consisting of a $FA_{0.7}Cs_{0.3}Pb(I_{0.7}Br_{0.3})_3$ perovskite layer sandwiched between two TaTm:F_6-TCNNQ (40 nm) transport layers (Figure S3a, Supporting Information). The *J*–*V* curves under illumination of the photoconductor (Figure S3b, Supporting Information) show a high current density under illumination, and a two order of magnitude lower dark current. In this device type, the current is mainly a hole current due to the p-type contact used, although some recombination at the organic/perovskite interface is expected in view of the use of non-selective transport layers. The hysteresis in between the scans in forward and reverse bias direction is likely related to the latter phenomenon, and partially to the use of electrodes with different work functions (ITO vs. Ag).

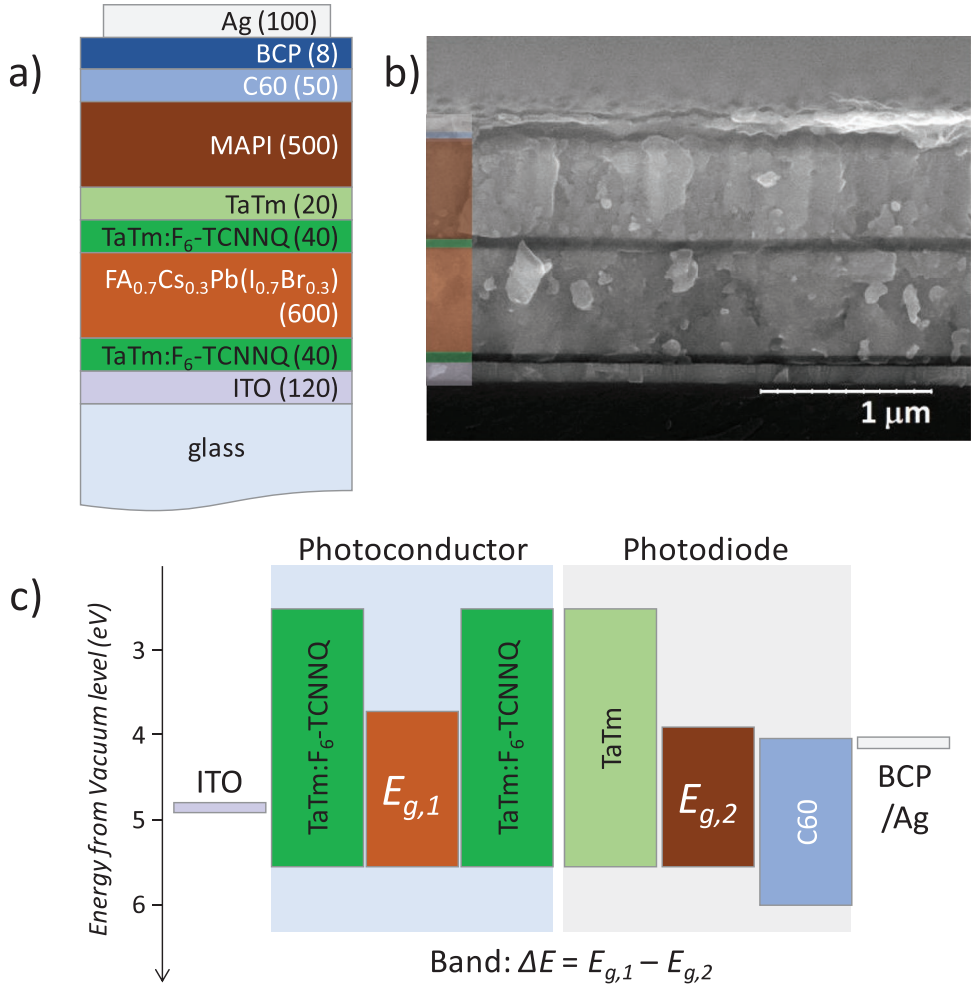

Figure 2. a) Schematic device structure of the tandem narrowband PD (layer thickness for each material is reported in nanometers). b) Cross-section of the device observed by SEM; scale bar corresponds to 1 µm. c) Approximate flat band energy diagram for the set of materials used in the narrowband PD.

The *J*–*V* characteristics of the narrowband PD in the dark and under illumination for bias voltages between –2 and 2 V, are illustrated in **Figure 3**a. The dark current is reduced in the tandem structure as compared to the isolated MAPI photodiode (Figure 1b), in particular in the –1 to 1 voltage range. The dark current density is 1.1×10^{-4} mA cm^{-2} at –1 V, and raises to 3.8×10^{-3} mA cm^{-2} at –2 V, closer to the value obtained for the MAPI photodiode at the same voltage. The more pronounced *J*–*V* hysteresis in between the forward and reverse (as compared to the isolated photodiode), is most likely related with the large hysteresis observed in the isolated photoconductor (Figure S3b, Supporting Information). The current density under illumination is 5.5 mA cm^{-2} at –1 V and virtually bias independent in the 0 to –2 voltage range. An interesting observation is the high V_{oc} obtained for the tandem photodiode (1.20 and 1.34 V in reverse and forward bias, respectively). This indicates that the V_{oc} of the two isolated subunits (1.0–1.1 and 0.1–0.3 V for the photodiode and photoconductor, respectively) is summed in the tandem architecture, as a consequence of the ohmic contact of this structure. The light/dark current ratio at –1 V exceeds four decades, which translates to a higher signal-to-noise ratio as compared to the MAPI photodiode. The spectral response of the tandem device is evaluated by measuring the EQE spectrum (Figure 3b). We observed a narrow peak in the EQE from 680 to 800 nm, with a weak shoulder at lower wavelength vanishing at 550 nm. Considering the bandgap of both perovskites (1.75 and 1.6 eV, corresponding to 708 and 775 nm, respectively), the wavelength difference in the spectral response is expected to be ≈70 nm. This agrees with the FWHM of the spectral response of the tandem photodiode, which varies from 61 to 82 nm depending on the applied bias voltage (Figure 3b). At the maximum of the response band, the EQE and responsivity (Figure S4, Supporting Information) values are above 58% and 0.32 A W^{-1}, respectively, between –2 and 0 V applied bias. The maximum EQE and responsivity at –1 V are 60% and 0.35 A W^{-1} (Figure 3c). We note that the EQE is varying with the applied bias, but not monotonically as one would expect if the photocurrent current would scale with the applied voltage. This can be partially ascribed to the electrical characteristics of the PD (Figure S3b, Supporting Information), leading to fluctuation in the photocurrent of the tandem device. Regarding the maximum measured EQE (0.68 at –2 V), it is

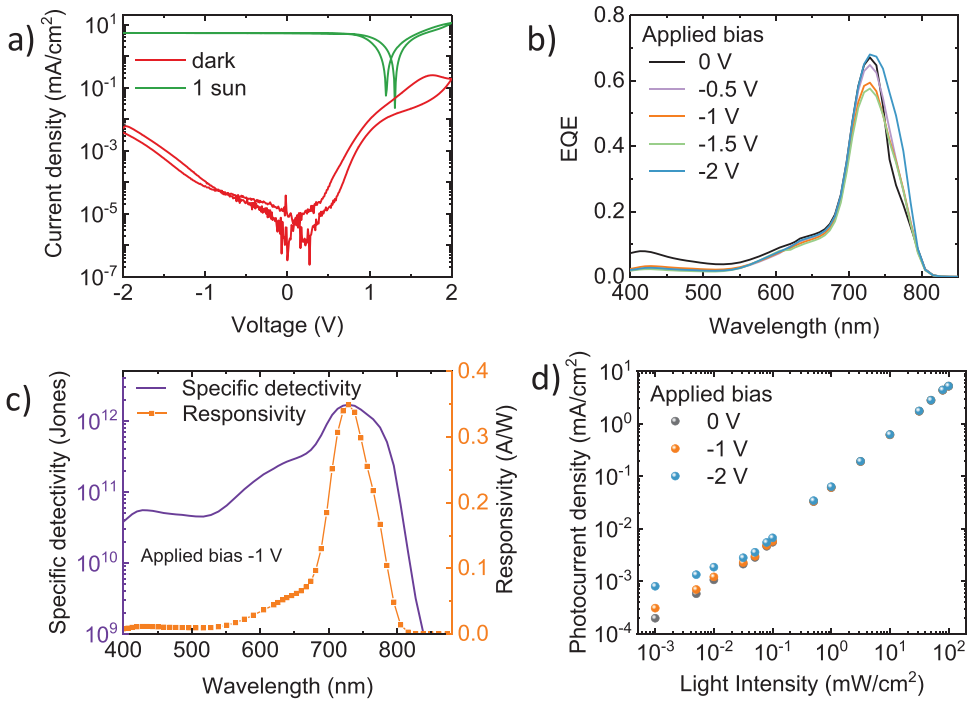

Figure 3. Characterization of the narrowband PD. a) *J–V* characteristics (–2 to 2 V) in the dark (red curve) and under 100 mW cm^{-2} illumination (green curve). b) EQE at different applied bias (–2 to 0 V, in 0.5 V step). c) Responsivity (orange line and symbols) and specific detectivity (purple curve) at –1 V. d) Dynamic response of the PD at different applied bias voltages.

lower as compared to the one of the MAPI photodiode at the same wavelength (above 0.8). This is expected as the absorption coefficient in perovskites is not abrupt, and the Urbach exponential tail will continue to absorb below the nominal bandgap value (1.75 eV) of the wide bandgap perovskite.[51] As Figure 3c illustrates, the maximum specific detectivity of the tandem device is 1.7×10^{12} Jones at 730 nm, when the applied bias is –1 V. When the thermal noise is the primary contribution of the noise (at zero bias condition), the specific detectivity of the narrowband PD increases to 6.1×10^{12} Jones at 730 nm (Figure S4, Supporting Information). Both values of the specific detectivity are comparable to best-in-class narrowband perovskite PDs reported so far.[7,33,52,53] The light intensity-dependent photocurrent at different applied bias voltages (0, –1, and –2 V) is illustrated in Figure 3d, showing a linear response to incident light from ≈3×10^{-2} to 10^2 mW cm^{-2} corresponding to a LDR for the narrowband PD of about 68 dB at 0 and –1 V, respectively. When the negative applied bias is increased to –2 V, the linear response to incident light is slightly reduced (from 5×10^{-2} to 10^2 mW cm^{-2}), resulting in a LDR of 63 dB.

Finally, in an attempt to further suppress the spectral response in the low-energy region of the visible spectrum (>550 nm, Figure 3b) of the tandem PD, the thickness of the wide bandgap perovskite in the photoconductor was increased from 600 nm to 1 µm. A cross-section SEM image of the narrowband PD incorporating a 1 µm wide bandgap perovskite layer in series with a 500 nm MAPI film is shown in **Figure 4**a. The corresponding *J–V* curves (between –2 and 2 V) in the dark and under illumination are shown in Figure 4b. Dark current values at –2 V are reduced from 3.8×10^{-3} to 1.8×10^{-4} mA cm^{-2}

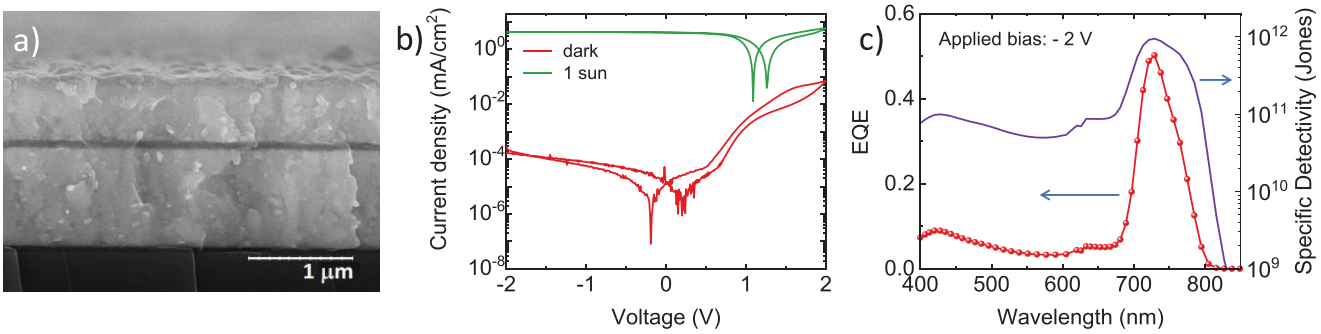

Figure 4. Characterization of the narrowband PD with thicker wide bandgap perovskite (1000 nm). a) Cross-section image of the tandem device as observed by SEM; scale bar corresponds to 1 µm. b) *J–V* characteristics (–2 to 2 V) in the dark (red curve) and under 100 mW cm^{-2} illumination (green curve). c) EQE (red line and symbols) and specific detectivity (purple line) measured at –2 V.

when the thickness of the front wide bandgap perovskite is increased from 600 to 1000 nm, respectively. The use of the thicker wide bandgap perovskite film mostly suppresses the PD response in the 550–700 nm range, and results in a narrower band in the NIR, albeit at the expense of a lower EQE (maximum 50% at 730 nm), due to the nature of the absorption coefficient in perovskites, as already discussed.

With the thick front perovskite, the FWHM is reduced from 77 to 69 nm at an applied bias of −2 V (Figure 4c). The lower dark current density at −2 V for the tandem PD with 1 µm thick perovskite film partially compensates for the lower EQE, leading to a specific detectivity of 9.5×10^{11} Jones at 730 nm, higher compared to the one of the detector with the 600 nm thick perovskite film (3×10^{11} Jones), at the same wavelength. Using the tandem approach, the spectral response of the narrowband detector can be varied by changing the chemical composition of the two perovskite films. To show this, we prepared a different tandem configuration which includes a $FA_{0.6}Cs_{0.4}Pb(I_{0.65}Br_{0.35})_3$ perovskite photoconductor (1.8 eV) in series with a triple cation $Cs_{0.3}(FA:MA)Pb(I_{0.8}Br_{0.2})_3$ perovskite photodiode (1.73 eV). These vacuum-deposited perovskite films have been recently reported by some of us (material characterization in Figure S5, Supporting Information).[51,54] First, we characterized the EQE of the standalone $Cs_{0.3}(FA:MA)Pb(I_{0.8}Br_{0.2})_3$ photodiode (Figure S6a, Supporting Information). The device shows the characteristic broadband EQE expected for a direct bandgap perovskite absorber. When placing the $FA_{0.6}Cs_{0.4}Pb(I_{0.65}Br_{0.35})_3$ photoconductor in series with the photodiode, we observe a suppression of the device response in the visible wavelength range (Figure S6b, Supporting Information). Importantly, the EQE peak is blue shifted at 700 nm compared to the $FA_{0.7}Cs_{0.3}Pb(I_{0.7}Br_{0.3})_3/MAPbI_3$ tandem, and due to the closer bandgaps of the two perovskite films, the FWHM is reduced to 30 nm.

A comparison of the key figures of merit of the tandem detector with other published narrowband perovskite photodiodes (Table S1, Supporting Information) shows that it can deliver high specific detectivity in spite of being driven at relatively high reverse bias. Depending on the combination of perovskite films used in the device, the FWHM also compares favorably with the literature. One drawback of this architecture is the non-zero spectral response in the UV–vis range, which in turns limits the rejection ratio. We noticed that high rejection ratios have been obtained with self-filtered detectors where the wide bandgap perovskite is not electrically integrated within the device.[33,11] This observation suggests that the limiting factor for the rejection ratio (i.e., the tandem detector showing weak but appreciable response in the UV–vis) might be related with the electrical connection between the two subunits (photoconductor and photodetector). To test this hypothesis, we fabricated a device with a perovskite film vacuum deposited on the glass side of the substrate, and compared it to the tandem configuration (Figure S7, Supporting Information). Indeed, we do see a suppression of the visible component when the wider bandgap perovskite is used as a filter on the glass side of the substrate, confirming that the photoconductor in the tandem configuration contributes to some extent to the spectral response of the tandem.

Finally, we tested the time response of the tandem detector and compared it with the single photodiode. As reported in Figure S8, Supporting Information, both the photodiode and the tandem photodetector can follow and resolve a laser excitation at 1 kHz, with 50% duty cycle. We did observe a capacitive current surge in the onset of the pulse, hence we analyzed the current fall when the laser switches off (at 500 µs). Indeed, we do observe a longer current decay in the tandem detector (the time to reach 10% of the initial maximum signal is 25.3 µs) as compared to the photodiode (3.2 µs). The longer discharge time can be associated to transport (transit time) but also to charge accumulation and or trapping within the tandem structure, due to the increased thickness and number of layers.

3. Conclusion

In conclusion, we show a new approach to obtain narrowband perovskite PDs. Using vacuum-deposited multilayers, we developed a tandem PD where a wide bandgap perovskite photoconductor is monolithically connected to a broadband perovskite photodiode. The narrow spectral response of the tandem devices is determined by the difference in the bandgaps of the perovskite employed as a photoconducting filter and the one used in the rear photodiode. In this proof-of-concept design, we achieved detectors with FWHM ranging from 30 to 80 nm, which is comparable to best-in-class previously reported perovskite PDs.[7,29,33,55] With this approach, the spectral response of the narrowband PD can be tuned by changing the bandgap of the wide bandgap perovskite used in the front photoconductor. These narrowband PDs have external quantum efficiencies up to 60% at 730 nm, low dark current and high specific detectivity in reverse bias. The proposed approach allows for easier encapsulation and integration of narrowband photodetectors in practical applications.

4. Experimental Section

Materials: *N4,N4,N4′,N4′*-tetra([1,1′-biphenyl]-4-yl)-[1,1′:4′,1″-terphenyl]-4,4′-diamine (TaTm) and 2,2′-(perfluoronaphthalene-2,6-diylidene) dimalononitrile (F_6-TCNNQ) were kindly provided by Novaled GmbH. Fullerene (C_{60}) was purchased from Merck KGaA and $CHNH_2NH_2I$ (FAI) from Greatcell Solar. CH_3NH_3I (MAI), PbI_2, and bathocuproine (BCP) were purchased from Luminescence Technology Corp. $PbBr_2$ was obtained from Tokyo Chemical Industry.

Device Fabrication: Pre-patterned ITO-coated glass substrates were subsequently cleaned with soap, water, and isopropanol in an ultrasonic bath, followed by a 20 min UV–ozone treatment. Substrates were transferred to a vacuum chamber integrated in a nitrogen-filled glovebox and evacuated to a pressure of 10^{-6} mbar. In general, the deposition rate for TaTm and C_{60} was 0.6 Å s^{-1} while the thinner BCP layer was sublimed at 0.2 Å s^{-1}. Ag was deposited in a second vacuum chamber using aluminum boat as source by applying currents ranging from 2.5 to 4.5 A. The deposition rate for the co-deposited doped layers was 0.8 Å s^{-1} for TaTm and 0.05 Å s^{-1} for the dopant (F_6-TCNNQ). The wide bandgap perovskites were deposited in a vacuum chamber equipped with four evaporation sources (Creaphys) and with independent temperature controllers, shutter, and QCM sensor, following a previously reported protocol.[51,54] For $MAPbI_3$ deposition, MAI and PbI_2 were co-evaporated simultaneously with rates of 0.6 and 1 Å s^{-1}, respectively. Two evaporation sources (one for PbI_2 and one for MAI) and three QCM sensors were used for $MAPbI_3$ deposition, where two controlled the deposition rate of the sources and the third one (close to the substrate holder) was used to monitor the total deposition rate. During the evaporation the pressure of the chamber was maintained at 5×10^{-6} mbar. The devices were encapsulated with epoxy resin inside a glovebox. A commercial

Araldite two-component epoxy resin (2014-2) was spread at the edges of a square 4.8 cm^2 aluminum plate, with bent edges of 1 mm height, then centered at the device substrate, fully covering the evaporated area inside the resin/aluminum perimeter. The resin was cured for 4 h.

Characterization: SEM images were performed on a Hitachi S-4800 microscope operating at an accelerating voltage of 2 kV over platinum metallized samples. The *J–V* curves of the PDs were recorded with a Keithley 2612A SourceMeter in a −2 and 2 V voltage range with 0.01 V steps and were illuminated under a Wavelabs Sinus 70 LED solar simulator using a custom LabVIEW program. The light intensity was calibrated before every measurement using a calibrated Si reference diode. Intensity-dependent data were carried out by measuring *J–V* curves in the same system using neutral density filters of decreasing optical density. In the EQE measurements the device was illuminated with a Quartz-Tungsten-Halogen lamp (Newport Apex 2-QTH) through a monochromator (Newport CS130-USB-3-MC), a chopper at 279 Hz and a focusing lens. The device current was measured as a function of energy from 3.5 to 2.0 eV in 0.05 eV steps and from 2.0 to 1.4 eV in 0.02 eV steps using a lock-in amplifier (Stanford Research Systems SR830). The system was calibrated, and the solar spectrum mismatch was corrected using a calibrated Si reference cell. The time response of the photodiodes was measured by illuminating the devices with a MatchBox laser pulsed at 1 kHz and 50% duty cycle. The signal of the photodetector was monitored with a Rohde & Schwarz RTM3004 Oscilloscope (1 GHz) through an input resistance of 50 Ω.

Supporting Information

Supporting Information is available from the Wiley Online Library or from the author.

Acknowledgements

We acknowledge Jorge Ferrando for his help and expertise in the device characterization. The authors acknowledge support from the Comunitat Valenciana (PROMETEU/2020/077), the Ministry of Science and Innovation (MCIN), and the Spanish State Research Agency (AEI). Project RTI2018-095362-A-I00 funded by MCIN/AEI/10.13039/501100011033 and by "ERDF A way of making Europe." Project PCI2020-112084 and grant IJCI-2019-039851-I funded by MCIN/AEI/10.13039/501100011033 and by the "European Union NextGenerationEU/PRTR"; Grant PRE2019-091181 and RYC-2016-21316 funded by MCIN/AEI/10.13039/501100011033 and by "ESF Investing in your future"; Grant CEX2019-000919-M funded by MCIN/AEI/10.13039/501100011033.

Conflict of Interest

The authors declare no conflict of interest.

Data Availability Statement

The data that support the findings of this study are available from the corresponding author upon reasonable request.

Keywords

narrowband photodetection, perovskites, photodetectors, tandem devices, vacuum deposition

Received: May 6, 2022
Revised: June 30, 2022
Published online:

[1] F. Wang, X. Zou, M. Xu, H. Wang, H. Wang, H. Guo, J. Guo, P. Wang, M. Peng, Z. Wang, Y. Wang, J. Miao, F. Chen, J. Wang, X. Chen, A. Pan, C. Shan, L. Liao, W. Hu, *Adv. Sci.* **2021**, *8*, e2100569.
[2] F. P. García de Arquer, A. Armin, P. Meredith, E. H. Sargent, *Nat. Rev. Mater.* **2017**, *2*, 16100.
[3] H. Wang, D. H. Kim, *Chem. Soc. Rev.* **2017**, *46*, 5204.
[4] G. Konstantatos, E. H. Sargent, *Nat. Nanotechnol.* **2010**, *5*, 391.
[5] H. Ren, J. De Chen, Y. Q. Li, J. X. Tang, *Adv. Sci.* **2021**, *8*, 2002489.
[6] G. Simone, M. J. Dyson, S. C. J. Meskers, R. A. J. Janssen, G. H. Gelinck, *Adv. Funct. Mater.* **2020**, *30*, 1904205.
[7] Z. Liu, L. Tao, Y. Zhang, G. Zhou, H. Zhu, Y. Fang, G. Wu, D. Yang, H. Chen, *Adv. Opt. Mater.* **2021**, *9*, 2100288.
[8] J. Xue, Z. Zhu, X. Xu, Y. Gu, S. Wang, L. Xu, Y. Zou, J. Song, H. Zeng, Q. Chen, *Nano Lett.* **2018**, *18*, 7628.
[9] L. Wang, Z. Li, M. Li, S. Li, Y. Lu, N. Qi, J. Zhang, C. Xie, C. Wu, L.-B. Luo, *ACS Appl. Mater. Interfaces* **2020**, *12*, 21845.
[10] L. Shen, Y. Zhang, Y. Bai, X. Zheng, Q. Wang, J. Huang, *Nanoscale* **2016**, *8*, 12990.
[11] S. Qiao, Y. Liu, J. Liu, G. Fu, S. Wang, *ACS Appl. Mater. Interfaces* **2021**, *13*, 34625.
[12] M. Dandin, P. Abshire, E. Smela, *Lab Chip* **2007**, *7*, 955.
[13] E. Cicek, R. McClintock, C. Y. Cho, B. Rahnema, M. Razeghi, *Appl. Phys. Lett.* **2013**, *103*, 181113.
[14] A. Sobhani, M. W. Knight, Y. Wang, B. Zheng, N. S. King, L. V. Brown, Z. Fang, P. Nordlander, N. J. Halas, *Nat. Commun.* **2013**, *4*, 1643.
[15] Y. Dong, Y. Gu, Y. Zou, J. Song, L. Xu, J. Li, J. Xue, X. Li, H. Zeng, *Small* **2016**, *12*, 5622.
[16] B. Siegmund, A. Mischok, J. Benduhn, O. Zeika, S. Ullbrich, F. Nehm, M. Böhm, D. Spoltore, H. Fröb, C. Körner, K. Leo, K. Vandewal, *Nat. Commun.* **2017**, *8*, 15421.
[17] Z. Tang, Z. Ma, A. Sánchez-Díaz, S. Ullbrich, Y. Liu, B. Siegmund, A. Mischok, K. Leo, M. Campoy-Quiles, W. Li, K. Vandewal, *Adv. Mater.* **2017**, *29*, 1702184.
[18] R. D. Jansen-van Vuuren, A. Armin, A. K. Pandey, P. L. Burn, P. Meredith, *Adv. Mater.* **2016**, *28*, 4766.
[19] C. Zhang, T. Shen, D. Guo, L. Tang, K. Yang, H. Deng, *InfoMat* **2020**, *2*, 1034.
[20] X. K. Liu, W. Xu, S. Bai, Y. Jin, J. Wang, R. H. Friend, F. Gao, *Nat. Mater.* **2021**, *20*, 10.
[21] J. Miao, F. Zhang, *J. Mater. Chem. C* **2019**, *7*, 1741.
[22] H. Wang, S. Li, X. Liu, Z. Shi, X. Fang, J. He, *Adv. Mater.* **2021**, *33*, 2003309.
[23] A. Kojima, K. Teshima, Y. Shirai, T. Miyasaka, *J. Am. Chem. Soc.* **2009**, *131*, 6050.
[24] J. Jeong, M. Kim, J. Seo, H. Lu, P. Ahlawat, A. Mishra, Y. Yang, M. A. Hope, F. T. Eickemeyer, M. Kim, Y. J. Yoon, I. W. Choi, B. P. Darwich, S. J. Choi, Y. Jo, J. H. Lee, B. Walker, S. M. Zakeeruddin, L. Emsley, U. Rothlisberger, A. Hagfeldt, D. S. Kim, M. Grätzel, J. Y. Kim, *Nature* **2021**, *592*, 381.
[25] M. I. Saidaminov, M. A. Haque, M. Savoie, A. L. Abdelhady, N. Cho, I. Dursun, U. Buttner, E. Alarousu, T. Wu, O. M. Bakr, *Adv. Mater.* **2016**, *28*, 8144.
[26] R. Ollearo, J. Wang, M. J. Dyson, C. H. L. Weijtens, M. Fattori, B. T. van Gorkom, A. J. J. M. van Breemen, S. C. J. Meskers, R. A. J. Janssen, G. H. Gelinck, *Nat. Commun.* **2021**, *12*, 7277.
[27] Z. Li, X. Liu, C. Zuo, W. Yang, X. Fang, *Adv. Mater.* **2021**, *33*, 2103010.
[28] A. Armin, R. D. Jansen-van Vuuren, N. Kopidakis, P. L. Burn, P. Meredith, *Nat. Commun.* **2015**, *6*, 6343.
[29] Q. Lin, A. Armin, P. L. Burn, P. Meredith, *Nat. Photonics* **2015**, *9*, 687.
[30] Y. Fang, Q. Dong, Y. Shao, Y. Yuan, J. Huang, *Nat. Photonics* **2015**, *9*, 679.
[31] H.-S. Rao, W.-G. Li, B.-X. Chen, D.-B. Kuang, C.-Y. Su, *Adv. Mater.* **2017**, *29*, 1602639.

[32] J. Li, J. Wang, J. Ma, H. Shen, L. Li, X. Duan, D. Li, *Nat. Commun.* **2019**, *10*, 806.
[33] L. Li, Y. Deng, C. Bao, Y. Fang, H. Wei, S. Tang, F. Zhang, J. Huang, *Adv. Opt. Mater.* **2017**, *5*, 1700672.
[34] D. Tordera, B. Peeters, H. B. Akkerman, A. J. J. M. Breemen, J. Maas, S. Shanmugam, A. J. Kronemeijer, G. H. Gelinck, *Adv. Mater. Technol.* **2019**, *4*, 1900651.
[35] J. Ávila, C. Momblona, P. P. Boix, M. Sessolo, H. J. Bolink, *Joule* **2017**, *1*, 431.
[36] P. Du, L. Wang, J. Li, J. Luo, Y. Ma, J. Tang, T. Zhai, *Adv. Opt. Mater.* **2022**, *10*, 2101770.
[37] C. Momblona, L. Gil-Escrig, E. Bandiello, E. M. Hutter, M. Sessolo, K. Lederer, J. Blochwitz-Nimoth, H. J. Bolink, *Energy Environ. Sci.* **2016**, *9*, 3456.
[38] J. Avila, L. Gil-Escrig, P. P. Boix, M. Sessolo, S. Albrecht, H. J. Bolink, *Sustainable Energy Fuels* **2018**, *2*, 2429.
[39] R. A. Z. Razera, D. A. Jacobs, F. Fu, P. Fiala, M. Dussouillez, F. Sahli, T. C. J. Yang, L. Ding, A. Walter, A. F. Feil, H. I. Boudinov, S. Nicolay, C. Ballif, Q. Jeangros, *J. Mater. Chem. A* **2020**, *8*, 242.
[40] L. Bertoluzzi, J. B. Patel, K. A. Bush, C. C. Boyd, R. A. Kerner, B. C. O'Regan, M. D. McGehee, *Adv. Energy Mater.* **2021**, *11*, 2002614.
[41] A. R. Bowring, L. Bertoluzzi, B. C. O'Regan, M. D. McGehee, *Adv. Energy Mater.* **2018**, *8*, 1702365.
[42] A. Pierre, A. C. Arias, *Flexible Printed Electron.* **2016**, *1*, 043001.
[43] D. Tordera, A. J. J. M. van Breemen, A. J. Kronemeijer, J.-L. van der Steen, B. Peeters, S. Shanmugan, H. B. Akkerman, G. H. Gelinck, *Organic Flexible Electron: Fundamentals, Devices, and Applications*, Elsevier, The Netherlands **2021**, pp. 575.
[44] S. van Reenen, M. Kemerink, H. J. Snaith, *J. Phys. Chem. Lett.* **2015**, *6*, 3808.
[45] P. Calado, A. M. Telford, D. Bryant, X. Li, J. Nelson, B. C. O'Regan, P. R. F. Barnes, *Nat. Commun.* **2016**, *7*, 13831.
[46] S. Xing, V. C. Nikolis, J. Kublitski, E. Guo, X. Jia, Y. Wang, D. Spoltore, K. Vandewal, H. Kleemann, J. Benduhn, K. Leo, *Adv. Mater.* **2021**, *33*, 2102967.
[47] C. Bao, Z. Chen, Y. Fang, H. Wei, Y. Deng, X. Xiao, L. Li, J. Huang, *Adv. Mater.* **2017**, *29*, 1703209.
[48] C. Liu, K. Wang, C. Yi, X. Shi, P. Du, A. W. Smith, A. Karim, X. Gong, *J. Mater. Chem. C* **2015**, *3*, 6600.
[49] B. R. Sutherland, A. K. Johnston, A. H. Ip, J. Xu, V. Adinolfi, P. Kanjanaboos, E. H. Sargent, *ACS Photonics* **2015**, *2*, 1117.
[50] F. Palazon, D. Pérez-del-Rey, B. Dänekamp, C. Dreessen, M. Sessolo, P. P. Boix, H. J. Bolink, *Adv. Mater.* **2019**, *31*, 1902692.
[51] L. Gil-Escrig, C. Dreessen, F. Palazon, Z. Hawash, E. Moons, S. Albrecht, M. Sessolo, H. J. Bolink, *ACS Energy Lett.* **2021**, *6*, 827.
[52] J. Wang, S. Xiao, W. Qian, K. Zhang, J. Yu, X. Xu, G. Wang, S. Zheng, S. Yang, *Adv. Mater.* **2021**, *33*, 2005557.
[53] Y. Hou, C. Wu, X. Huang, D. Yang, T. Ye, J. Yoon, R. Sriramdas, K. Wang, S. Priya, *Adv. Funct. Mater.* **2021**, *31*, 2007016.
[54] I. Susic, L. Gil-Escrig, F. Palazon, M. Sessolo, H. J. Bolink, *ACS Energy Lett.* **2022**, *7*, 1355.
[55] Z. Lan, L. Cai, D. Luo, F. Zhu, *ACS Appl. Mater. Interfaces* **2021**, *13*, 981.